Acta Geotechnica
https://doi.org/10.1007/s11440-025-02784-8

RESEARCH PAPER

Study on mechanical properties of fly ash and coir fiber improved expansive soil subgrade

L. H. Li[1] · T. Ning[1] · Z. Q. Zhan[2] · Y. L. Gui[3] · C. Zhang[1]

Received: 10 December 2024 / Accepted: 18 September 2025

Abstract
Fly ash and coir fiber are solid waste materials commonly used to mitigate the swelling and shrinkage of expansive soil subgrades. While prior research has primarily explored their individual effects, the combined influence of these materials remains underexplored. Through compaction and unconfined compressive strength tests, this study investigated the coupled effects of fly ash and coir fiber content, along with curing time, on the mechanical properties of expansive soil, addressing this critical research gap. The results demonstrate that the addition of fly ash and coir fibers significantly enhances the unconfined compressive strength of expansive soil, with peak strength achieved at fly ash and coir fiber contents of 20 and 0.5%, respectively. Furthermore, the unconfined compressive strength increases notably with longer curing times. Building on the findings from element tests, physical model tests (static and dynamic loading tests) were further conducted to study the mechanical response of improved expansive soil subgrades under geosynthetic reinforcement conditions, such as geogrids and geocells. The optimal embedment depth of the geosynthetics is approximately 0.33 times the width of the foundation. Compared to unreinforced subgrades, the settlement of reinforced subgrades is significantly reduced. Including geosynthetics demonstrates notable diffusion and attenuation effects on vertical stress and peak acceleration, respectively. Furthermore, the stress distribution angle of geocell-reinforced subgrades is higher than that of geogrid-reinforced subgrades, indicating a more pronounced effect on subgrade reinforcement.

Keywords Coir fiber · Expansive soil · Fly ash · Geosynthetics · Physical model tests

1 Introduction

Expansive soils are widely recognized as a global geotechnical challenge, characterized by significant volume changes with variations in moisture content. Their swelling and shrinkage properties can cause severe damage to engineering infrastructures, particularly in railway and highway subgrades [1–3]. Therefore, developing cost-effective and reliable improvement methods to enhance the bearing capacity of expansive soils, as well as their ability to accommodate complex loads, is critically important.

Over the past few decades, many studies have focused on controlling the swelling and shrinkage behavior of expansive soils to enhance their strength [4, 5]. Various

✉ Z. Q. Zhan
zhiqizhan@polyu.edu.hk

L. H. Li
lilihua466@163.com

T. Ning
1870275006@qq.com

Y. L. Gui
yilin.gui@qut.edu.au

C. Zhang
374436698@qq.com

[1] Key Laboratory of Health Intelligent Perception and Ecological Restoration of River and Lake, Ministry of Education, School of Civil Engineering, Architecture and Environment, Hubei University of Technology, Wuhan, China

[2] Department of Civil and Environmental Engineering, The Hong Kong Polytechnic University, Hung Hom, Kowloon, Hong Kong, China

[3] Group of Sustainable Engineered Construction Materials, Faculty of Engineering, Queensland University of Technology, Gardens Point, Brisbane, QLD 4000, Australia

Published online: 10 October 2025

improvement approaches, including physical and chemical methods, are widely used. Physical methods for improving expansive soils primarily involve techniques that enhance their density and drainage characteristics, such as compaction, drainage, and soil replacement [6–8]. However, these methods may not always be economically or practically feasible in engineering applications due to the large volumes of earth involved. Chemical methods primarily use various binders, such as lime and cement, to improve the strength of expansive soils [9, 10]. Nonetheless, this approach can lead to brittle behavior in the treated soils [11]. Additionally, these materials are not environmentally friendly, as the greenhouse gas emissions from cement and lime production contribute approximately 7–8% of global emissions [12, 13]. Therefore, it is crucial to reduce the production of traditional binders and to explore more sustainable materials.

Fly ash, primarily produced from coal-fired power plants, is a valuable sustainable material. Sivapullaiah et al. [14] demonstrated that the incorporation of fly ash increases the plastic limit of expansive soils due to its pozzolanic reactivity. Cokca [15] further established that fly ash stabilizes expansive soils by promoting the flocculation of dispersed clay particles through cation exchange mechanisms. Phani Kumar and Sharma [16] found that adding fly ash significantly increased the plastic limit and maximum dry unit weight of expansive soils while reducing the liquid limit and optimum moisture content. Zha et al. [17] explored the combined effects of fly ash and lime treatments, concluding that these additives can effectively reduce the swell potential and shrinkage of expansive soils. More recently, Li et al. [18] examined the mechanical properties, chemical reactions, and microstructural evolution of construction waste stabilized with alkali-activated fly ash. Their findings indicated that this approach enhances the maximum compressive strength and stability of subgrade fill.

Coir fiber is an economical and effective material for soil reinforcement. It possesses favorable tensile strength, stiffness, hydraulic properties, and long-term resistance to biodegradation [19–22]. Research by Sivakumar Babu and Vasudevan [23] and Sivakumar Babu et al. [24] indicates that the shear strength of soil increases with the content of coir fiber. This enhancement occurs because coir fibers improve friction and anchoring between soil particles. Maliakal and Thiyyakkandi [25] investigated the impact of coir fiber on the shear strength of clay. Their findings revealed that when the fiber content exceeds 1%, the shear strength of the soil begins to decline. Anggraini et al. [26] studied the tensile and compressive strengths of both natural and improved soft soils. They found that the addition of lime and coir fiber significantly enhances these strengths, particularly when the curing period is extended. The coir fibers contribute additional tensile and compressive strength to the soil.

Geosynthetics are widely used for subgrade reinforcement, and their properties significantly influence the reinforcement effectiveness. Wang et al. [27] found that the addition of geogrids can enhance the ultimate bearing capacity of foundations. However, increasing the number of reinforcement layers has limited effectiveness, because general failure occurs in soils with a single layer of reinforcement, while punching shear failure happens in other cases. Li et al. [28] demonstrated that the use of geosynthetic reinforcement significantly reduces the maximum vertical stress on subgrades. It also creates a more homogeneous stress distribution, leading to lower settlements and reduced horizontal deformations. Baadiga et al. [29] reported that geogrid reinforcement significantly increases rut depth through interlocking and lateral restraint of aggregates. Stiff geogrids distribute applied loads over a wider area at the subgrade level, minimizing rutting depths. Raja and Shukla [30] found that wraparound geosynthetic reinforcement can significantly improve foundation bearing capacity and reduce settlement. This improvement is attributed to the additional lateral restraint and frictional resistance provided by geosynthetics, which also enhance soil compaction.

In summary, incorporating fly ash and coir fiber as partial replacements in expansive soil improvement can effectively enhance subgrade strength by mitigating swelling and shrinkage behavior, and promoting the resourceful utilization of solid waste. Prior studies have primarily focused on the individual effects of fly ash and coir fiber, but there is limited research on the combined use of these two materials in expansive soil subgrades. To address this research gap, this study investigated the effects of fly ash and coir fiber on the mechanical properties of expansive soils through compaction tests and unconfined compression tests, ultimately determining the optimal ratio of fly ash to coir fiber. Additionally, the mechanical response of improved expansive soil subgrades (treated by fly ash and coir fiber with optimal ratio) was evaluated under various geosynthetic reinforcement conditions through physical model tests. The performance of geocell reinforcement was compared to both unreinforced conditions and geogrid reinforcement, aiming to assess the effectiveness of the reinforced subgrades. These findings offer innovative, eco-friendly solutions for subgrades design, advancing sustainable geotechnical engineering practices.

2 Test methods

In this study, compaction tests and unconfined compression tests were conducted to evaluate the effects of fly ash and coir fiber on the mechanical properties of expansive soils, as well as to determine the optimal ratios of these materials. Additionally, the mechanical response of the improved expansive soil subgrade was assessed under various geosynthetic reinforcement conditions through modeling tests. It is important to note that both static and dynamic loading scenarios are considered in physical model tests.

2.1 Materials

The expansive soil used in this study was collected from Wuhan, China, at a sampling depth of 2.0–2.5 m below the ground surface. The physical properties of the soil samples were assessed, and specific parameters are presented in Table 1.

The fly ash utilized in this study is from a power plant in Wuhan, China. It is light gray in color and classified as Class C fly ash. The C-class fly ash used contains lime as alkaline activators, and the main component of lime is CaO, with a content of 1.92%. These activators are introduced via dry mixing of fly ash into the soil. The modification mechanism involves hydration and pozzolanic reactions, producing cementitious substances with flaky and cluster structures that adhere to soil particles, fill interparticle pores, and enhance soil density and skeleton strength, thereby improving overall soil mass strength [15, 17, 31, 32]. The chemical composition is presented in Table 2, while the particle size distribution can be referenced in Li et al. [33].

The coir fiber used in this study is from coconuts grown on Hainan Island, China. The physical properties of the coir fiber are presented in Table 3, while the test materials are illustrated in Fig. 1.

Figure 2 shows the structural configurations of biaxial geogrid, triaxial geogrid, and geocell. (a) Biaxial geogrid features a grid-like structure with equal strength in two perpendicular directions, typically used for soil stabilization and load distribution in pavements. (b) Triaxial geogrid has a triangular aperture pattern, providing enhanced load distribution and stability in multiple directions, making it suitable for heavy-duty applications. (c) Geocell consists of interconnected three-dimensional cells that confine soil, offering superior reinforcement for subgrades and retaining wall. The biaxial geogrid, triaxial geogrid, and geocell used in the physical model tests are consistent with those employed in [28, 33, 34]. The main technical specifications are presented in Table 4.

To ensure the validity of geogrid scaling in the model tests, similarity principles based on dimensional analysis were adopted, following Buckingham's π theorem [35], to scale key parameters such as geometric dimensions, stiffness, and tensile strength. A scaling ratio of N = 3 was applied, with geometric dimensions scaled by N, and both stiffness and forces (e.g., tensile strength) scaled by N^2, in accordance with established practices for geosynthetic-reinforced soil models. Huang et al. [36] utilized a similar scaling approach (N = 2) for geogrid-reinforced bridge abutments, scaling stiffness and strength by N^2 to maintain dynamic similarity in load transfer. Mehrjardi and Khazaei [37] performed 36 repeated plate load tests with a scaling ratio of N = 3.5, demonstrating that scaled geogrid parameters effectively replicated prototype behavior, with load–settlement responses within 10% of full-scale results. In this study, geogrid parameters were selected to align with these scaled values, ensuring consistency with the referenced studies. Due to experimental constraints, direct validation tests for scaling effects were not conducted. Future research will include additional tests to further validate the scaling effects.

Studies demonstrate that the reinforcement method adapted in this study is cost-effective due to reduced material use and enhanced performance. Sharma et al. [38]

Table 1 Physical properties of expansive soil

Natural moisture content (%)	21.2
Optimum moisture content (%)	19.6
Maximum dry density (g/cm^3)	1.71
Liquid limit (%)	51.2
Plastic limit (%)	23.4
Plastic index	27.8
Free swelling ratio (%)	52

Table 2 Chemical properties of fly ash

	Content (%)
SiO_2	60.64
Fe_2O_3	6.85
Al_2O_3	22.22
CaO	1.92
MgO	1.16
SO_3	0.16
K_2O	2.46
Na_2O	0.50
TiO_2	1.18
Others	0.15
Loss	2.74

Table 3 Physical properties of coir fiber

Length (mm)	20–25
Diameter (mm)	0.35
Density (g/cm^3)	1.74
Tensile strength (MPa)	150
Breaking elongation (%)	25

found that biaxial geogrid reinforcement increased road surface strength by 40% and reduced costs by 5% through life-cycle analysis. Mahdi et al. [39] showed that geogrids extend maintenance cycles, cutting costs by 36.67%. Poorahong et al. [40] noted that triaxial geogrids improve bearing capacity by 44% while reducing material costs. Tafreshi and Dawson [41] demonstrated that geocell reinforcement achieves up to 85% better bearing capacity with one-third the material of planar geotextiles. Lal et al. [42] confirmed higher bearing capacity ratios (7.92 vs. 5.83) using cost-effective, locally available materials, supporting the economic and performance benefits of geocell reinforcement.

2.2 Equipment

The compaction test uses the DZY-III multifunctional electric compactor to perform light compaction on the specimens, achieving an accuracy of better than ± 1% of the reading. This process aims to determine the optimum water content and maximum dry density of the expansive soil.

The unconfined compression test employs the WDW-10E microcomputer-controlled electronic testing machine. This equipment has a maximum load capacity of 20 kN (17,644 kPa) and maintains a constant load rate of 1 mm/min, with the test concluding upon reaching the peak value of the stress–strain curve.

In the physical model tests, the DNYS-200 is utilized to simulate traffic loads, the accuracy is better than ± 1% of the reading. This equipment primarily consists of a loading system, modeling system, circulation system, and monitoring system. It is capable of applying a maximum static vertical load of 100 kN (4444 kPa) and a maximum vertical displacement of 150 mm. The model box used for the test is a rigid box of 1800 mm (length) × 800 mm (width) × 1200 mm (height), which is made of glass. The surfaces of

Fig. 1 Test materials: **a** expansive soil; **b** fly ash; and **c** coir fiber

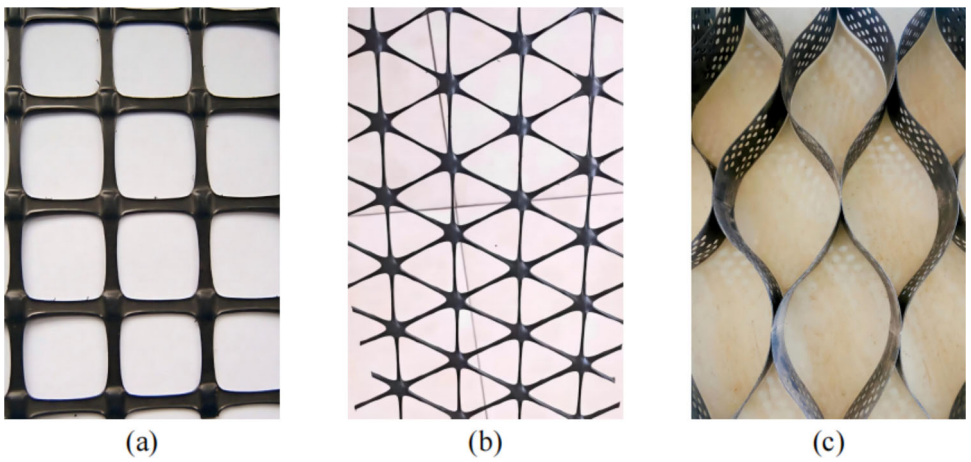

Fig. 2 Illustration of **a** biaxial geogrid; **b** triaxial geogrid; and **c** geocell

Table 4 Technical specifications of geosynthetics

Biaxial geogrid	
Mesh size length × width (mm)	40 × 40
Horizontal ultimate elongation (%)	13.2
Vertical ultimate elongation (%)	15.6
Horizontal ultimate tensile strength (kN/m)	20
Vertical ultimate tensile strength (kN/m)	20
Triaxial geogrid	
Horizontal ultimate elongation (%)	11.6
Vertical ultimate elongation (%)	10.6
Horizontal ultimate tensile strength (kN/m)	28.7
Vertical ultimate tensile strength (kN/m)	18.3
Geocell	
Height (mm)	50
Thickness (mm)	1
Tensile strength (MPa)	24
Breaking elongation (%)	9.8
Grid size (mm)	400 × 400

the model box are coated with Vaseline to minimize the influence of friction on the test results.

Nine miniature soil pressure sensors are employed to measure vertical stress within the subgrade in the physical model tests. These sensors have a measurement range of 0.01–20 MPa, with an accuracy of 0.5% FS (full scale) and an effective frequency range of 0–100 Hz. The settlement of the load plate is monitored using a displacement sensor integrated into the load system, while three LVDT linear displacement transducers are utilized to measure the settlement/rise at the top of the subgrade, with an accuracy of 0.01 mm. Additionally, five dynamic accelerometers are used to monitor the dynamic response of the subgrade soil. The measurement range of the accelerometers is 0 to 10 mV/(m/s^2), with an effective frequency range of 0.2–300 Hz, a sensitivity of 100 mV/(m/s^2), and a resolution of 0.1 mg. To ensure the accuracy of the readings, all sensors are calibrated prior to each series of tests.

In addition, during the loading process, data are tested using the DH5922D dynamic signal testing and analysis system, the strain gauge error is ± (0.5% red ± 3με), and the voltage gauge error is no more than 0.2% FS. This system is comprised of two main components: power supply and the dynamic data acquisition instrument. The dynamic data acquisition instrument features a total of 48 independent channels, each with a maximum sampling frequency of 1000 Hz. There is no limit to the number of channels, and data are collected at a frequency of 50 Hz during testing.

2.3 Test program

2.3.1 Compaction test

The expansive soil samples were dried at 105 °C and then sieved through a 2-mm sieve. An appropriate amount of dried expansive soil and fly ash is weighed to prepare soil mixtures with fly ash proportions of 0, 10, 20, 30, and 40%. The dimensions of the specimens are Φ38 mm × H76 mm. The maximum dry density and optimum water content of each soil mixture are determined through compaction tests.

2.3.2 Unconfined compression test

The unconfined compression tests were conducted under varying contents of fly ash (0%, 10%, 20%, 30%, 40%), coir fiber (0%, 0.25%, 0.5%, 1.0%), and curing time (1 day, 7 days, 14 days, 28 days). The fiber addition process began with mixing the soil and coir fiber to form homogeneous mixtures, avoiding the addition of water initially to prevent fiber clumping and ensure proper dispersion. Water was then gradually introduced to achieve the target moisture content, followed by additional mixing to produce uniform mixtures. All experiments were conducted in triplicate to ensure the reliability of the results, with a coefficient of variation less than 5%. All tests were performed at the optimum moisture content. The cylindrical specimens were prepared using a single compression molding method, achieving a density of 95% of the maximum dry density obtained from the compaction tests. The dimensions of the specimens are Φ38 mm × H76 mm. After demolding, the specimens were wrapped in cling film, sealed, and cured in a standard curing room (with a temperature of 23 ± 1 °C and a relative humidity of 98%) until the designated age to ensure the reliability of the data. Each group of specimens consisted of three identical samples, and the average values are used for analysis. The test program for the unconfined compression tests is summarized in Table 5.

2.3.3 Physical model test

The subgrade soil is a mixture of expansive soil, fly ash, and coir fiber, using the optimum mixing ratio determined by compaction test and unconfined compression test. The subgrade soil is evenly divided into four layers, each with a thickness of 200 mm, and the degree of compaction is at 95%.

As shown in Fig. 3, the square steel plate has a side length of 150 × 150 mm and a thickness of 20 mm. The size of the subgrade model is 1200 × 800 × 800 mm (length × width × height), which is more than five times the width of the load plate to minimize boundary effects

Table 5 Test program of the unconfined compression test

Sample code	Soil sample name	Fly ash content (%)	Coir fiber content (%)	Curing time (day)
U1	Pure soil	0	0	1, 7, 14, 28
U2	Improved soil	10	0	1, 7, 14, 28
U3		20	0	
U4		30	0	
U5		40	0	
U6	Improved soil	20	0.25	28
U7			0.5	
U8			1.0	

[42–44]. The load plate was positioned at the top center of the subgrade. It was leveled using a leveling tool to prevent tilting and ensure even load distribution. The bottom of the load plate is coated with epoxy resin adhesive and rolled in sand to create a rough surface. The ends are then coated with Vaseline to reduce lateral friction [41].

To accurately determine the static/dynamic response of the subgrades under different conditions, multiple earth pressure boxes and LVDT were laid in the model. Three LVDTs were set up at 0.5B (B = 150 mm), 1.5, and 2.5B from the center of the load plate to measure the settlement displacement/rise position at different locations during loading [45]. According to Li et al. [46] and Li et al. [33],

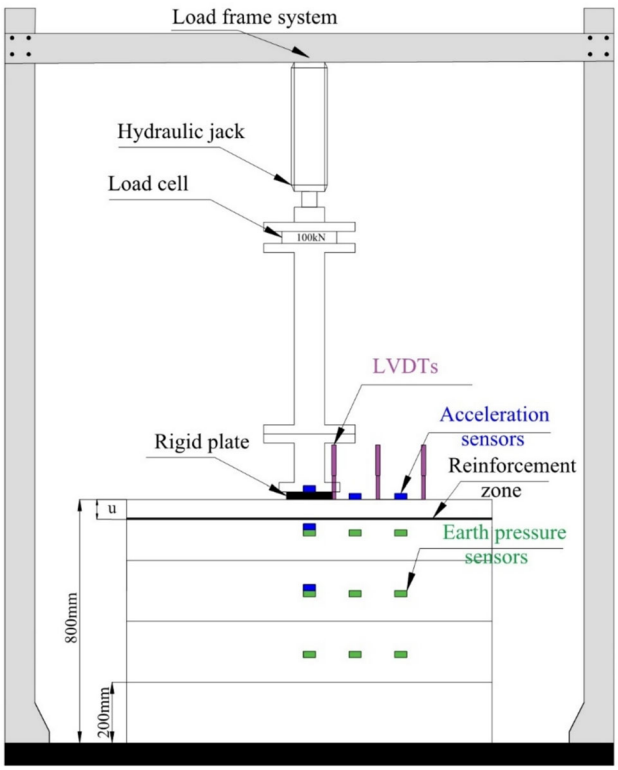

Fig. 3 Configuration of the physical model test

measurement sensors embedded within the range of 0 to 0.7 m from the top of the subgrade can effectively capture the static and dynamic responses. Therefore, one earth pressure box was placed in the middle of each layer, positioned 1.0 and 2.0B away from the center of the load plate. In total, three layers were used to measure the magnitude of vertical stresses at different locations within each layer of the subgrade soil. The accelerometers are horizontally arranged on the load plate at positions 1.0 and 2.0B from the center of the load plate. Additionally, they are vertically positioned below the load plate at depths of 100 and 300 mm to measure the acceleration at different locations within the subgrade soil layers. The specific locations of each monitoring sensor in the model are shown in Fig. 4 Due to the symmetry of the subgrade model, all sensors in this test were placed on one side of the model.

The model tests were conducted in three phases:

1) Static loading was applied to the subgrade model to determine the optimum depth for reinforcement placement. The optimal depth for the biaxial geogrid was assessed by placing it at various depths (u) from the top of the subgrade during three static loading tests.
2) Dynamic loading was performed on an unreinforced subgrade model to evaluate its dynamic response, including vertical stress, acceleration, and settlement/rise.
3) Dynamic loading tests were conducted with the reinforcement placed at the optimum depth identified in the static loading phase. This aimed to assess the effect of the reinforcement on the dynamic response of the subgrade.

Before each test, a vertical preload of 22 kPa was applied to the top of the subgrade. This ensured uniform contact between the load plate and the subgrade surface, verified the proper functioning of all sensors, and calibrated the readings to zero.

The test programs of static and dynamic loading are shown in Table 6 and Table 7, respectively. The processes of static loading and dynamic loading are as follows:

Static Loading: during the testing process, a hydraulic jack applies incremental loading through a rigid square steel plate (side length B = 150 mm). Each loading increment is 178 kPa and is maintained until the settlement of the load plate is less than 0.03 mm for six consecutive minutes, after which the next increment is applied. The test is stopped when the total settlement reaches 25% of the load plate width.

Dynamic Loading: a dynamic sinusoidal wave is used to simulate the dynamic loads transmitted by vehicles. The loading amplitudes are set at 267, 356, and 444 kPa (corresponding to 30, 40, and 50% of the unreinforced

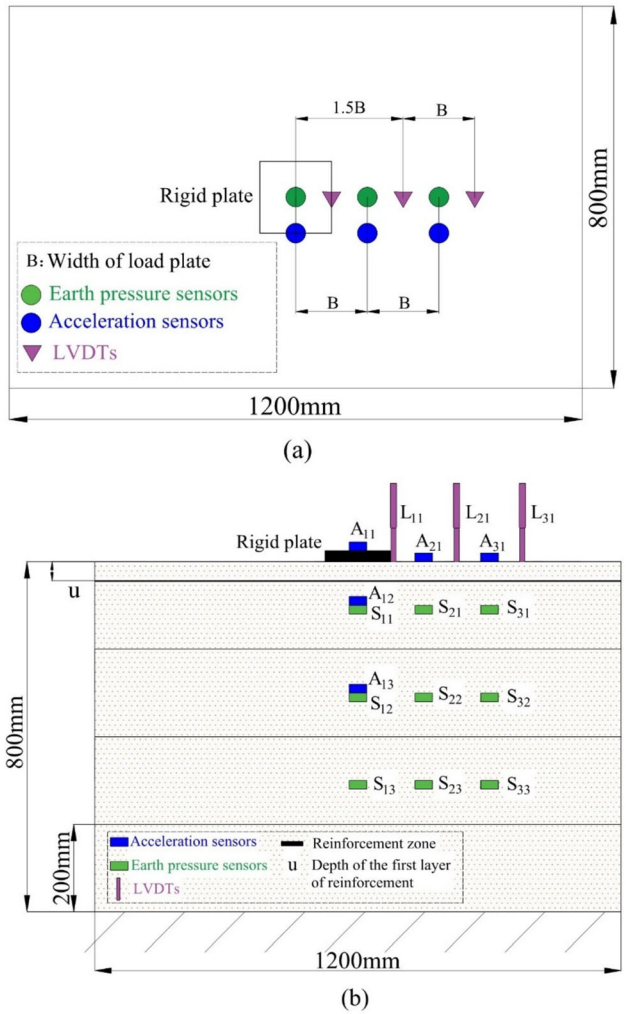

Fig. 4 **a** Plan layout and **b** cross-sectional layout of sensors

subgrade's ultimate bearing capacity, respectively). The frequency of the sinusoidal wave is set at 1 Hz, with a total of 1000 cycles.

3 Test results and analysis

3.1 Compaction tests

Figure 5 shows the relationship between dry density and moisture content for fly ash-expansive soil mixtures with varying fly ash dosages, as determined from compaction tests. In Fig. 5, "FA" denotes the fly ash dosage. It can be seen that the maximum dry density of pure soil (0% FA) is 1.71g/cm^3, and the optimum moisture content is 19.57%. With the increase of fly ash dosage, the maximum dry density of the mixture increases from 1.71 to 1.74 g/cm^3 (20% FA) and then decreases to 1.68 g/cm^3 (40% FA). The optimum water content decreases from 19.57 to 16.03% (20% FA), and then increases to 18% (40% FA). The optimum water content of soil mixture is the smallest (16.03%), and its maximum dry density is the largest (1.74 g/cm^3) when the fly ash dosage is 20%. This is because, at low fly ash content, the mixture has a lower affinity for water. As the fly ash content increases, the voids in the soil are filled, resulting in an increase in maximum dry density. The addition of fly ash alters the void structure of the soil, requiring less moisture to achieve optimum water content. However, as the fly ash content continues to increase, the specific gravity of the mixed soil decreases, causing soil particles to aggregate into larger clumps, which increases the voids between the fly ash and the soil, leading to a

Table 6 Static loading test program

Test series	Type of reinforcement	u/B
1	Unreinforced	/
2	Biaxial geogrid reinforced	0.16, 0.33, 0.67
3	Triaxial geogrid reinforced	0.33
4	Geocell reinforced	0.33

Table 7 Dynamic loading test program

Test series	Type of reinforcement	u/B	Amplitude (kPa)	Frequency (Hz)
1	Unreinforced	/	267	1
2			356	
3			444	
4	Biaxial geogrid	0.33	267	
5	Triaxial geogrid	0.33	267	
6	Geocell	0.33	267	

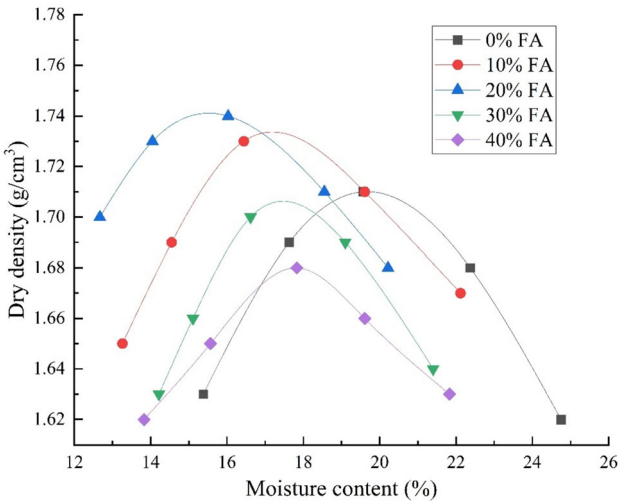

Fig. 5 Variation of dry density in expansive soils with different moisture content and fly ash dosages

decrease in maximum dry density. Furthermore, the increase in fine particle materials enlarges the specific surface area, necessitating more water to lubricate the soil particles, thereby resulting in an increase in optimum water content.

Although direct experimental data on the effects of coir fiber on the optimum moisture content and maximum dry density were not obtained in this study due to limitations, a review of existing literature provides insights into typical trends. The addition of coir fiber generally leads to a decrease by 2–3% in maximum dry density, attributed to the lower specific gravity of the fibers compared to soil particles, which reduces the overall density of the mixture. Conversely, the optimum moisture content tends to increase by 5–15% because of the high water absorption capacity of coir fibers, necessitating more moisture for effective compaction. These trends align with the expected behavior of the expansive soil used here. Future studies will include targeted compaction tests to validate these observations for the specific soil–fiber combinations used here [47, 48].

3.2 Unconfined compression tests

Figure 6 presents the unconfined compressive strength (UCS) of the mixtures at various fly ash dosages over different curing times. It can be observed that the UCS value increases with the increase in fly ash dosage (0–20%). This is due to the fly ash reaction that forms hydrated calcium silicate (C-S–H). The C-S–H gel binds the soil particles together, creating a strong fly ash-expansive soil matrix that enhances the compressive strength of the improved soil. When the fly ash dosage exceeds 20%, the fly ash particles replace the expansive soil particles, resulting in a decrease in the UCS value.

Furthermore, the UCS of improved soil remains consistently higher than that of pure soil. Additionally, the UCS of the improved soil increases with the duration of curing time. The addition of 20% fly ash raises the UCS value from 562.7 to 901.6 kPa after 1 day maintenance. After 28-day maintenance, the UCS value increases to 2067.3 kPa. This increase is attributed to the growth of hydration gel over time. This process is illustrated in Eqs. (1)–(4).

$$CaO + H_2O \rightarrow Ca(OH)_2 \quad (1)$$

$$Ca(OH)_2 \rightarrow Ca^{2+} + 2(OH)^- \quad (2)$$

$$Ca^{2+} + 2(OH)^- + SiO_2 \rightarrow C - S - H \quad (3)$$

$$Ca^{2+} + 2(OH)^- + Al_2O_3 \rightarrow C - A - H \quad (4)$$

Figure 7 shows the effect of different coir fiber dosages on the UCS of the expansive soil mixture with 20% fly ash

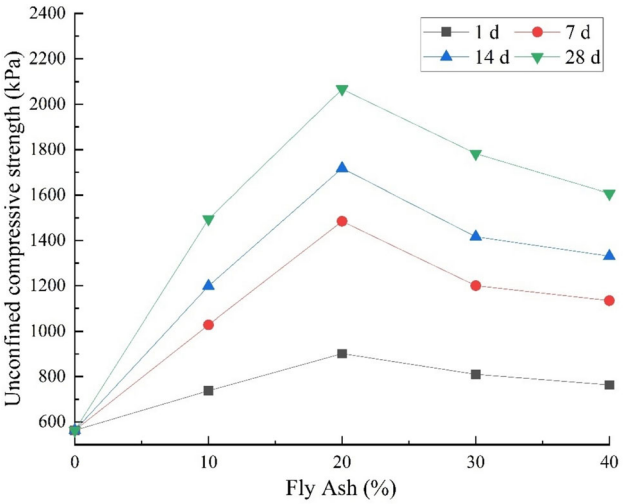

Fig. 6 Variation of unconfined compressive strength in expansive soils with different fly ash dosages and curing times

(optimal value) after 28 days of curing. It can be observed that the UCS value increases with the increase in coir fiber dosage (0–0.5%) first. This is due to the bonding effect between the soil particles and the fibers, which enhances the UCS. However, when the coir fiber dosage exceeds 0.5%, the UCS value decreases. This is because a high amount of fibers can adhere to each other, reducing the bonding between soil particles.

In this study, correlation analyses were performed separately for the effects of fly ash and coir fiber on UCS. Correlation analysis involves examining two or more related variables to assess the degree of association between them. The correlation coefficient (r) indicates the strength of the linear relationship between two variables: the closer the absolute value of r is to 1, the stronger the

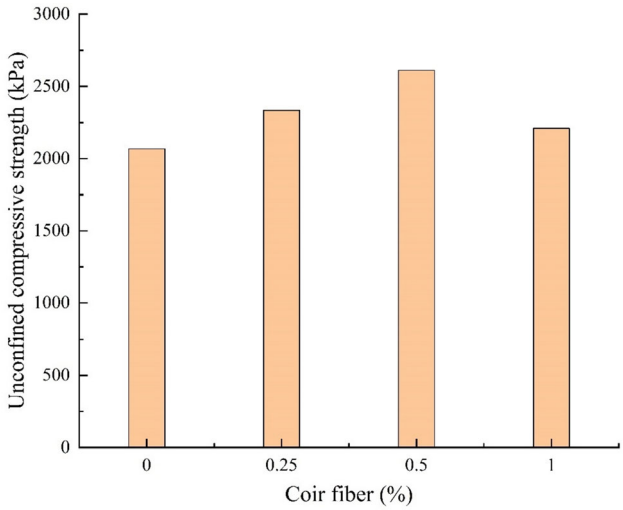

Fig. 7 Variation of unconfined compressive strength in fly ash-expansive soil mixture with different coir fiber dosages

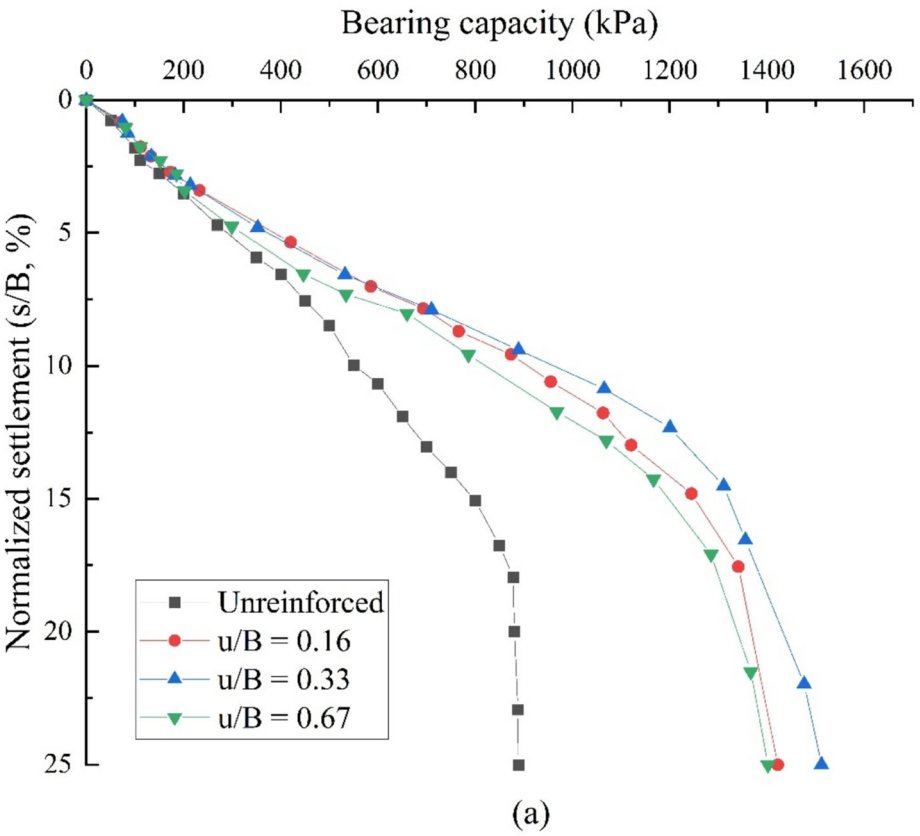

Fig. 8 Loading–settlement curves: **a** effects of burial depths with biaxial geogrid; **b** comparison of different geosynthetics at u = 0.33b

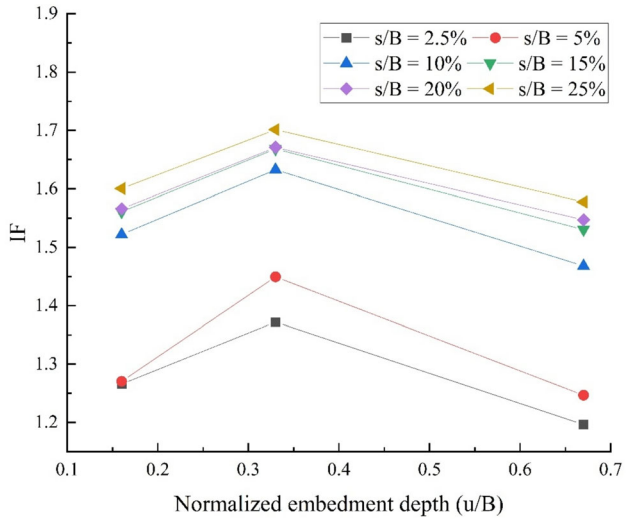

Fig. 9 Variation of improvement factors with different embedment at various settlements

linear relationship; the closer it is to 0, the weaker the relationship. The significance coefficient (p-value) is used to determine whether the correlation between two variables is statistically significant. When the p-value is less than a predetermined significance level (such as 0.05 or 0.01), the correlation is considered statistically significant. The correlation coefficient for fly ash was r = 0.998 with a significance value of p = 0.037 (< 0.05), while for coir fiber, the correlation coefficient was r = 0.999 with a significance value of p = 0.006. These results indicate that coir fiber has a more pronounced effect on UCS compared to fly ash.

In summary, the combination of expansive soil with 20% fly ash and 0.5% coir fiber results in the maximum improvement in UCS, as the interaction between fly ash and coconut fibers effectively enhances the strength of the expansive soil.

3.3 Static loading tests

3.3.1 Settlement

Figure 8 shows the loading–settlement curves of expansive soil mixed with 0.5% of coir fibers and 20% of fly ash (optimum mixing ratio) under different types of reinforcement. To minimize size effects, the settlement (s) is normalized by the width of the load plate (B).

Figure 8a presents the loading–settlement curves for biaxial geogrid reinforcement at different normalized embedded depths (u/B). It can be observed that the performance of the reinforced subgrade is superior to that of the unreinforced subgrade. The bearing capacity of the reinforced subgrade initially increases and then decreases with increase in embedment depth of the biaxial geogrid. The bearing capacity peaks at 1512.4 kPa with u = 0.33B, as shown in Fig. 8a, outperforming u/B = 0.16 and 0.67. This depth optimizes load distribution and soil–geogrid interaction, while shallower depths lack reinforcement and deeper ones reduce effectiveness due to deformation [6, 49, 50]. Thus, u = 0.33B is the optimal initial embedment depth among the three tested values.

Figure 8b shows the loading–settlement curves of subgrades at the optimal initial embedment depth (u = 0.33B) with different reinforced types (geosynthetics). It is evident that the bearing capacity of all reinforced subgrades is higher than that of the unreinforced subgrade. The order of bearing capacity for the reinforced subgrades is as follows: biaxial geogrid < triaxial geogrid < geocell. When the settlement ratio (s/B) is 25%, the bearing capacities of the biaxial geogrid-reinforced subgrade, triaxial geogrid-reinforced subgrade, and geocell-reinforced subgrade increase by 70, 72, and 88%, respectively. Among the different geosynthetics, geocell performs the best. This is because, even under small strains, the internal friction resistance of the geocell is fully activated. The grid walls of the geocell lock into the coir fiber-reinforced soil, creating a three-dimensional confinement effect.

It can also be observed that the loading–settlement curves for both unreinforced and reinforced subgrades exhibit linear behavior in the early stages of loading. As the load increases, shear failure occurs in the soil, and the curves become noticeably steeper, with rapid increases in settlement. This indicates that for single-layer reinforced soil subgrades, there is a prolonged range of elastic deformation, followed by a shorter range of plastic deformation, ultimately leading to sudden failure [27, 51].

3.3.2 Improvement factor

In this study, a dimensionless parameter, improvement factor (IF), is introduced to quantify the enhancement of bearing capacity characteristics.

$$IF = \frac{q_g}{q_0} \tag{5}$$

where: q_0 and q_g are the bearing capacity of unreinforced and reinforced subgrades for a given settlement (s/B = 2.5%, 5%, 10%, 15%, 20%, 25%), respectively.

Figure 9 shows the variation of IF with u/B for biaxial geogrid-reinforced subgrades at different settlements. It can be observed that the IF is greater than 1 in all cases. The reinforcing effect of the material occurs almost instantaneously, even at settlement ratios as low as 2.5–5%. This phenomenon occurs because the presence of geosynthetic prevents lateral expansion of the soil mass, which increases the soil's bearing capacity.

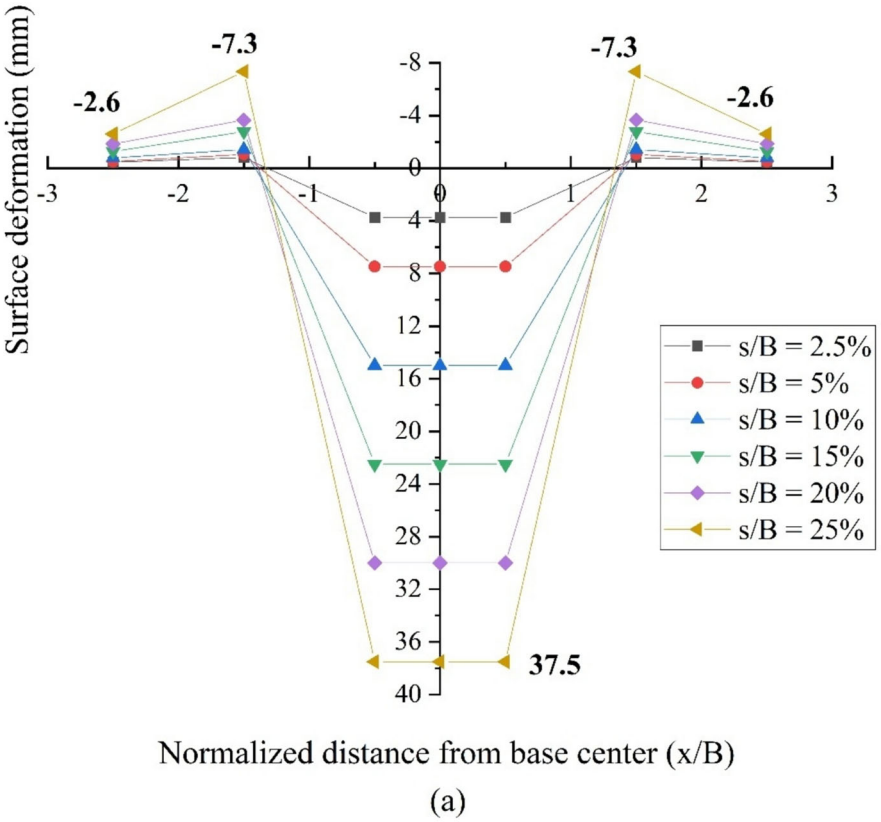

(a)

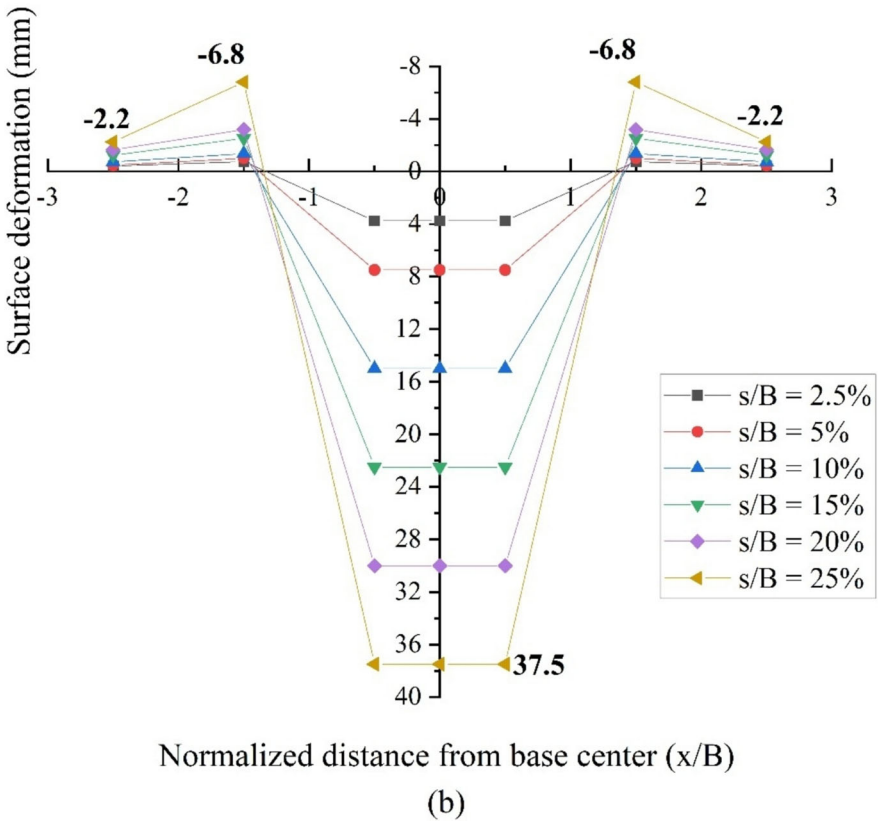

(b)

Fig. 10 Soil surface deformation profile with different normalized settlements: **a** unreinforced subgrade; **b** biaxial geogrid-reinforced subgrade; **c** triaxial geogrid-reinforced subgrade; **d** geocell-reinforced subgrade

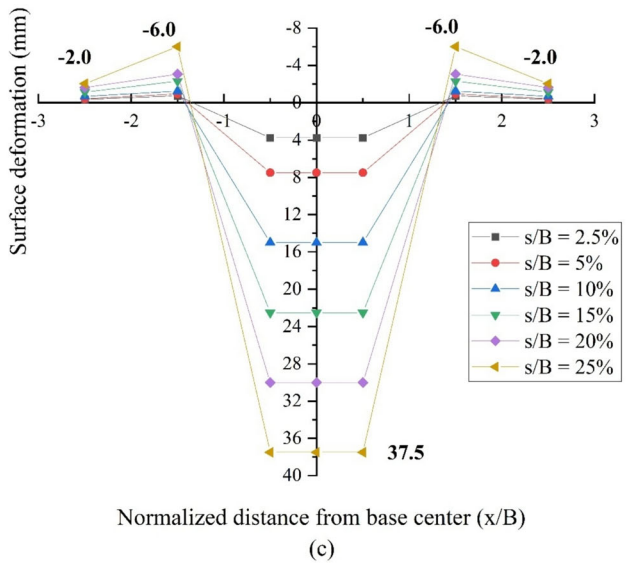

(c)

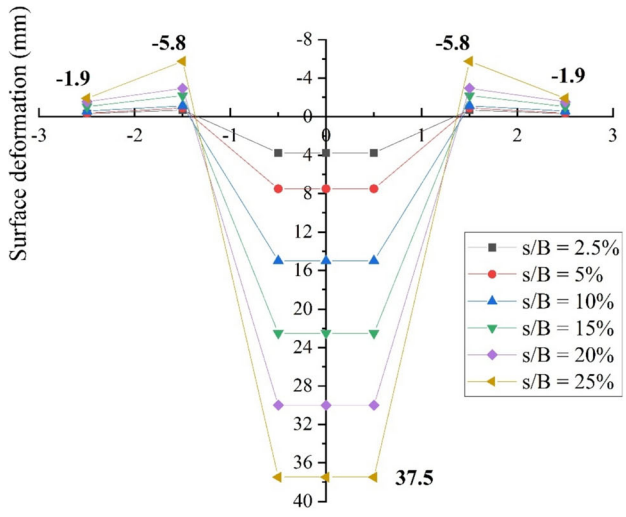

(d)

Fig. 10 continued

The IF increases with u/B, reaching its maximum value at u/B = 0.33 for all s/B cases. This is because the soil layer above the reinforcement acts as a barrier, preventing interaction between the reinforcement and the load plate, and distributes the footing pressure more evenly over the biaxial geogrid. When u/B is less than 0.33, the reinforcement layer is insufficient to generate interfacial frictional resistance, leading to lower bearing capacity values. After reaching the maximum performance improvement, the IF decreases with further increases in u/B. This occurs because the reinforcement is buried too deep, beyond the effective region, and cannot prevent lateral expansion of the soil when pressure is applied. Therefore, in this study, the geosynthetics were set at u/B = 0.33 in all cases.

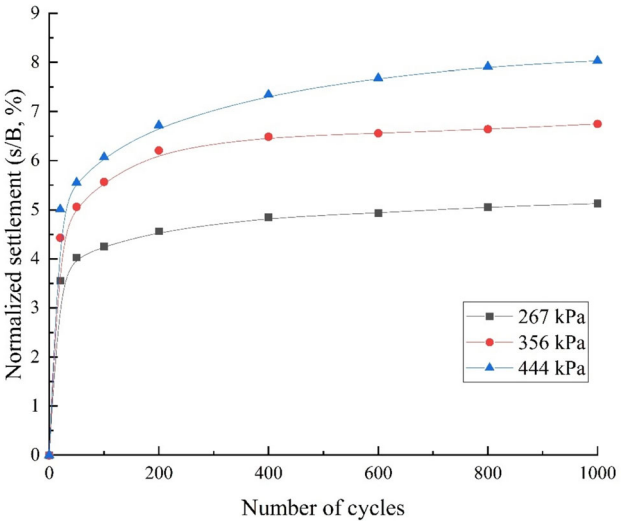

Fig. 11 Variation of settlement with the number of cycles at different amplitudes

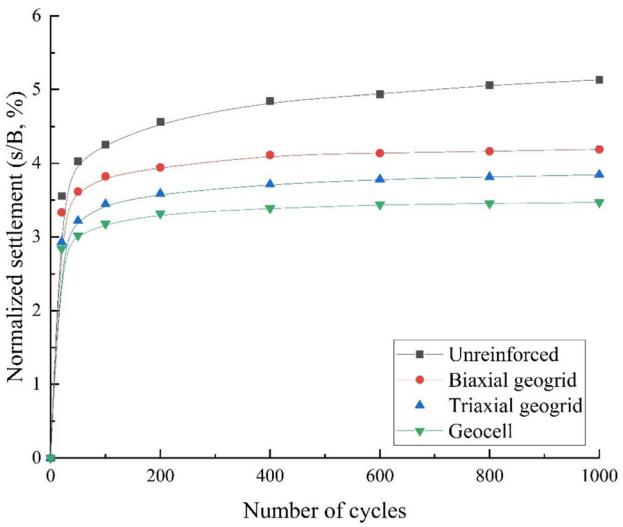

Fig. 12 Variation of settlement with the number of cycles in unreinforced and reinforced subgrades

Table 8 Nonlinear curve fitting results and settlement stabilization cycles for various reinforcement types

	Unreinforced	Biaxial geogrid	Triaxial geogrid	Geocell
a	2.81	2.90	2.49	2.49
b	0.09	0.06	0.07	0.05
R^2	0.9847	0.9502	0.9566	0.9567
C	600	600	400	200

3.3.3 Surface deformation

Figure 10 shows the distribution of surface deformation along the horizontal profile during loading for both

unreinforced and reinforced subgrades at different settlement ratios. In this study, negative values of soil surface deformation indicate uplift of the subgrade, while positive values indicate settlement. The numerical labels in Fig. 10 represent the surface deformation at typical locations.

Figure 10 reveals that surface deformation for both unreinforced and reinforced subgrades extends from the center of the subgrade to 2.5B. The maximum deformation occurs at a distance of 1.5B from the center of the load plate, with the incremental value at 1.5B significantly greater than that at 2.5B. As settlement ratio increases, the magnitude of surface deformation also increases. This is due to shear failure of the subgrade, which causes the soil to be displaced laterally.

Additionally, it can be observed that the inclusion of geosynthetics significantly reduces the surface deformation of the subgrade. The geosynthetics enhance the overall stiffness and strength of the subgrade, transforming the reinforced area into a semi-rigid foundation and altering the failure zone of the subgrade, effectively distributing pressure within the subgrade. Compared to unreinforced subgrades and geosynthetic-reinforced subgrades, the soil surface deformation in geocell-reinforced subgrades is smaller. This is attributed to the confinement effect of the geocell, which restricts soil particle movement and distributes the load to deeper soil layers, acting as a rigid foundation layer and preventing surface uplift.

3.4 Dynamic loading tests

3.4.1 Settlement

This study examines the effect of loading cycle numbers on the performance of unreinforced and reinforced subgrades. The maximum number of loading cycles is limited to 1000, with a sine wave frequency set at 1 Hz to observe general trends. Figure 11 shows the relationship between the number of loading cycles and settlement for unreinforced subgrades under different amplitudes (267 kPa, 356 kPa, 444 kPa). It can be observed that an increase in loading amplitude directly leads to an increase in settlement of the unreinforced subgrade. Additionally, during the first 200 loading cycles, both low and high amplitude loading resulted in significant settlement. This may be attributed to the rearrangement of soil particles during the cyclic loading–unloading process, leading to soil densification. As the number of loading cycles increases, the rate of cumulative settlement gradually slows down, and the slope of settlement becomes approximately horizontal by the end of the loading cycles (N = 1000). This result indicates that the soil undergoes strain hardening. Similar results were also obtained by Raja and Shukla [30].

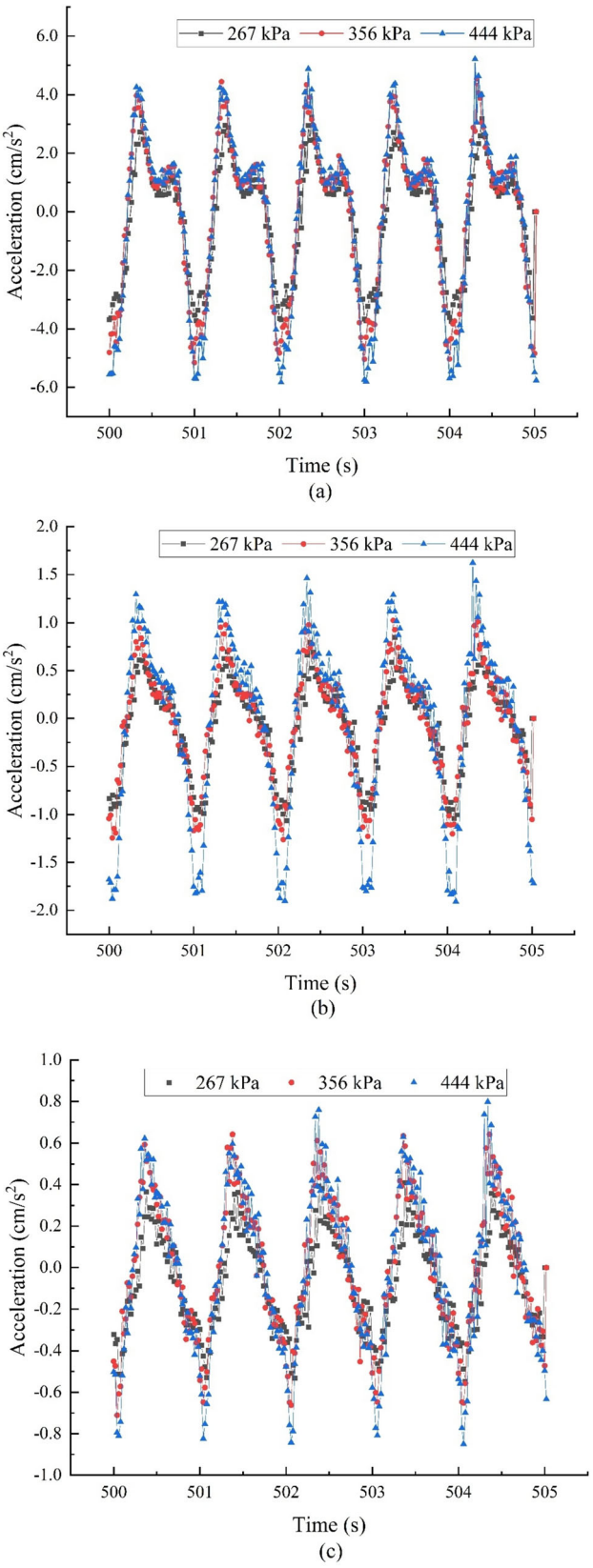

Fig. 13 Acceleration of the unreinforced subgrade under different load amplitudes at various locations: **a** A11; **b** A21; and **c** A31

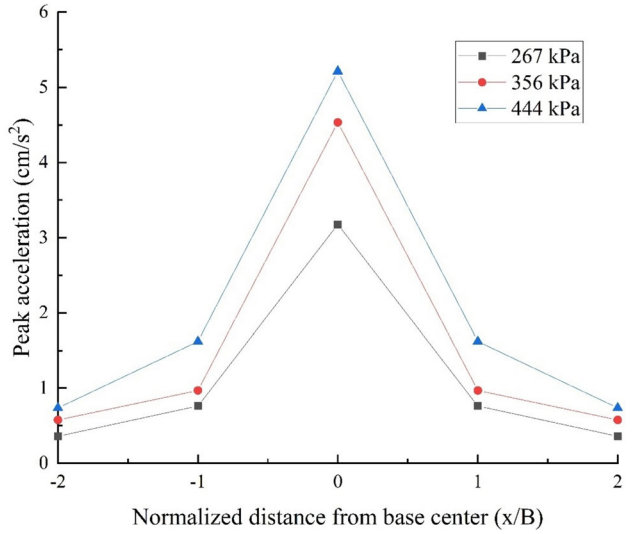

Fig. 14 Horizontal distribution of peak acceleration (unreinforced subgrade)

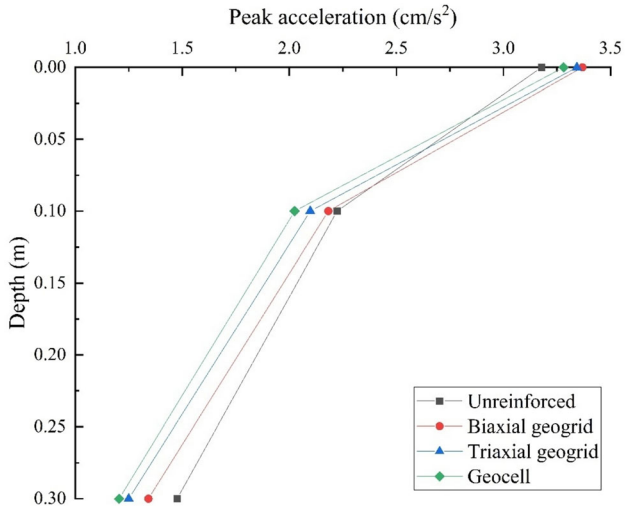

Fig. 15 Vertical distribution of peak acceleration (267 kPa)

Figure 12 shows the variation of settlement with the number of cycles for unreinforced and reinforced subgrades under a loading amplitude of 267 kPa. It can be observed that the settlement of the load plate increases with the number of loading cycles. The inclusion of geosynthetic significantly reduces the settlement of the load plate. At the end of the loading cycles (N = 1000), the settlement ratio for the unreinforced subgrade is 5.13%. Under the same conditions, the settlement ratios for subgrades reinforced with biaxial geogrid, triaxial geogrid, and geocell at N = 1000 are 4.19, 3.85, and 3.47%, respectively. This represents reductions of 18.34, 25.04, and 32.40% compared to the unreinforced subgrade. This improvement is attributed to the geosynthetic, which suppress the lateral movement of soil particles under increasing loading cycles.

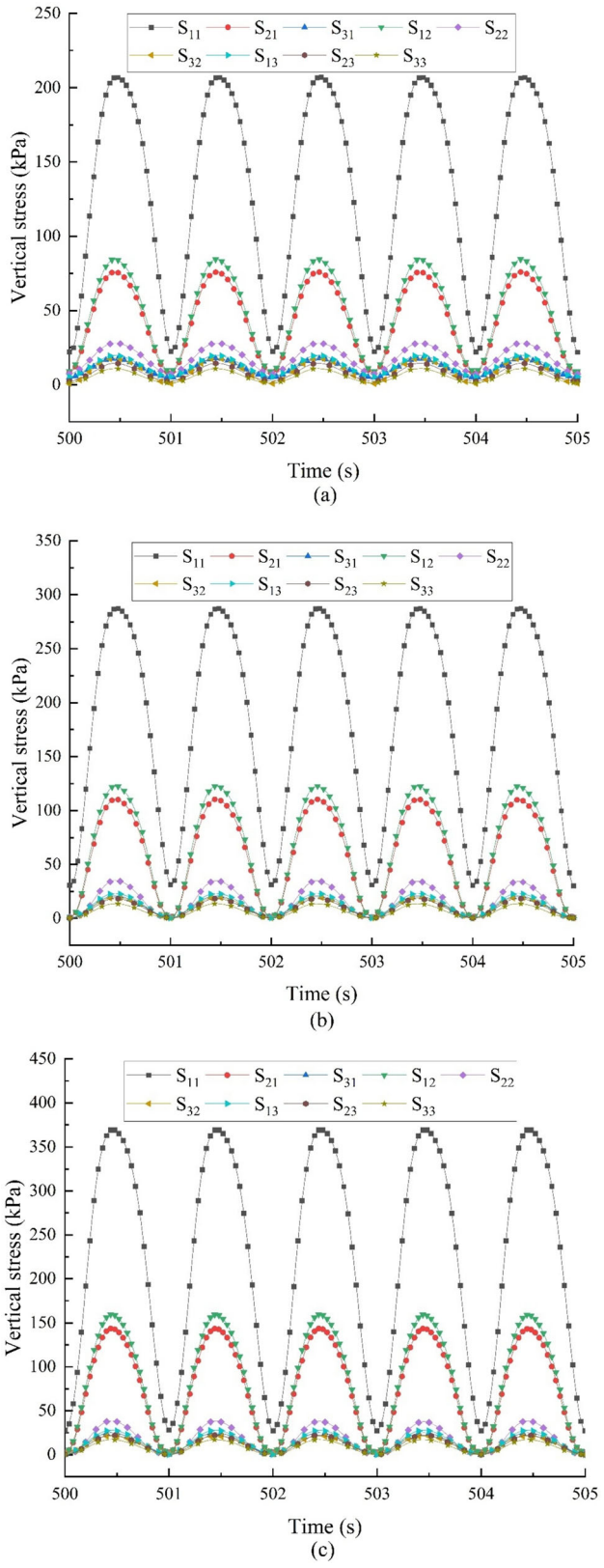

Fig. 16 Vertical stress time history curve of unreinforced subgrade under different load amplitudes: **a** 267 kPa; **b** 356 kPa; and **c** 444 Pa

The geocell provides three-dimensional structural support, while the geogrid layer interlocks with the membrane, acting as a rigid layer that reduces settlement under cyclic loading. Observations indicate that geosynthetic can significantly inhibit lateral dispersion of soil particles and resist applied loads [50–52, 55]. Among the three types of geosynthetics, geocell reinforcement is the most effective in limiting settlement of the subgrade under cyclic loading.

Nonlinear curve fitting for Fig. 12 was conducted using a power function model (allometric model), resulting in an equation of the form $y = ax^b$, where x represents the number of cycles and y is the normalized settlement. The fitting parameters are provided in * MERGEFORMAT Table 8. The goodness of fit was evaluated using the coefficient of determination (R^2), which measures how well the model explains the variability in the observed data. R^2 values range from 0 to 1, with values closer to 1 indicating stronger explanatory power and better fitting performance. As shown in * MERGEFORMAT Table 8, all R^2 values indicate good fitting results.

Figure 12 shows that the slope of the curve gradually approaches zero, indicating that after a certain number of cycles, the settlement increment becomes negligible with further loading. In this study, parameter C is defined as the number of cycles after which the settlement increment is less than 4%. According to * MERGEFORMAT Table 8, the C value is the smallest for the geocell-reinforced subgrade, demonstrating that geocell reinforcement is the most effective in reducing settlement increments and provides the most significant reinforcement performance.

3.4.2 Acceleration

Figure 13 shows the acceleration magnitudes at different locations of the subgrade under various loading amplitudes. The test results reveal that the acceleration data exhibit significant fluctuations and periodic phenomena at different load amplitudes. The peak and trough values of acceleration appear in pairs, with the response frequency matching the load frequency. As the load amplitude increases, the acceleration magnitude also increases significantly, indicating that load amplitude affects subgrade vibrations.

To study the lateral distribution of acceleration in the subgrade, acceleration values were monitored and compared at the center of the load plate, 1.0 and 2.0 B, based on peak dynamic responses, as shown in Fig. 14. It can be observed that the acceleration gradually decreases in the horizontal direction as the distance from the center of the load plate increases. For example, under a load of 444 kPa, the peak acceleration at the center of the load plate is 5.22 cm/s^2. At 1.0 B, the peak acceleration decreases by 68.9%, and at 2.0B, it decreases by 85.9%. This is because the vibrations generated in the subgrade soil propagate outward from the center, resulting in reduced acceleration. Additionally, the initial slope of the acceleration curves in Fig. 14 becomes steeper with increase in load magnitude, indicating an increased rate of acceleration decay. This may be due to soil densification caused by the increased load, leading to a rapid decrease in acceleration.

Accelerations at various depths of the subgrade were measured and analyzed based on peak dynamic responses. The effects of different geosynthetics on the acceleration response were also investigated. Figure 15 shows the peak acceleration responses at various depths directly beneath

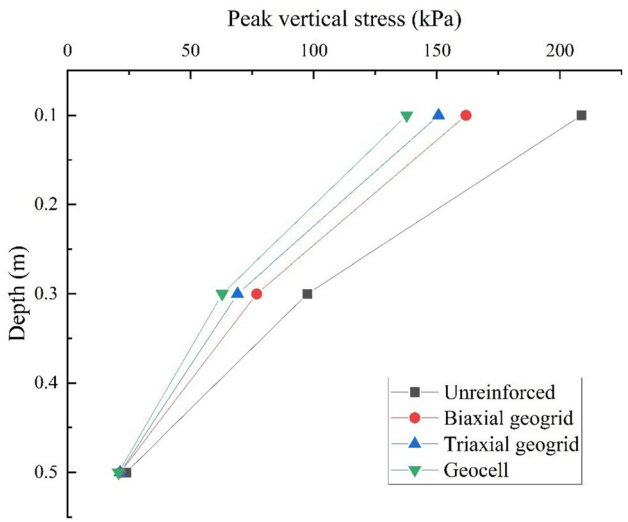

Fig. 17 Peak vertical stress response of unreinforced and reinforced subgrades at different depths

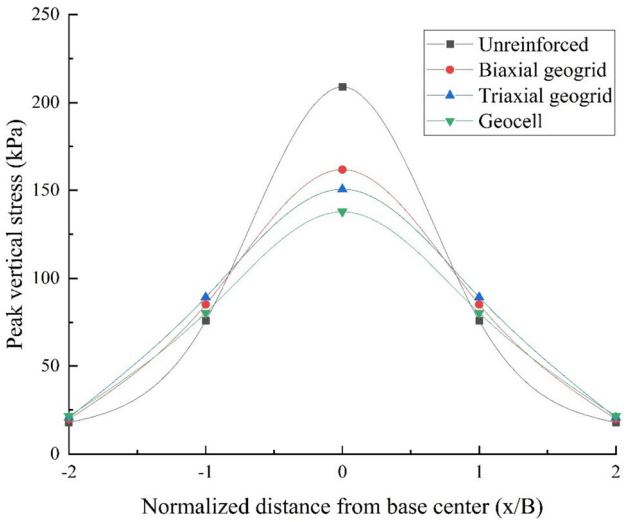

Fig. 18 Horizontal distribution of peak vertical stress in unreinforced and reinforced subgrades

the load plate under a 267 kPa load. It can be observed that the peak accelerations for both unreinforced and reinforced subgrades decrease with increase in depth. As depth increases, the peak accelerations for the unreinforced, biaxial geogrid-reinforced, triaxial geogrid-reinforced, and geogrid-reinforced subgrades decrease by 53.6, 60.2, 62.6, and 63.2%, respectively.

Compared to the unreinforced subgrade, the peak accelerations within the reinforced subgrade are all lower, indicating that the use of geosynthetics can reduce the dynamic effects of soil under cyclic loading. Further comparative analysis shows that the peak acceleration of the geocell-reinforced subgrade is significantly lower than that of the biaxial and triaxial geogrid-reinforced subgrades, demonstrating its superior seismic performance. This is primarily due to the three-dimensional mechanism of the geocell: the cell walls prevent the enclosed soil particles from moving laterally due to applied loads and lateral displacements, thereby increasing overall shear strength, redistributing the load within the confined area, and reducing acceleration.

3.4.3 Vertical stress

Figure 16 shows the variation of vertical stress with time in unreinforced subgrades under different load magnitudes. In Fig. 16, the labels S11 to S33 indicate monitoring points, as shown in Fig. 4b, and not components of the stress tensor. It can be observed that the vertical stress exhibits a half-sine wave pattern, with relatively stable peaks between adjacent waves, and the response frequency matches the loading frequency. As the load magnitude increases, the vertical stress at different locations also rises. When the load increases from 267 to 444 kPa, the peak vertical stress in S11 increases by 28 and 44%, respectively. This indicates that the internal pressure of the subgrade is significantly influenced by the magnitude of the load. Additionally, it is evident that the peak vertical stress decreases with increase in depth of the subgrade. When the load is 267 kPa, the vertical stress at depths of 10, 30, and 50 cm below the center of the load plate decreases from 206 to 19 kPa. This suggests that more vibrational energy is absorbed in the upper layers near the top of the subgrade. As the depth increases, the lower layers are gradually affected by the upper load, leading to a load dispersion effect.

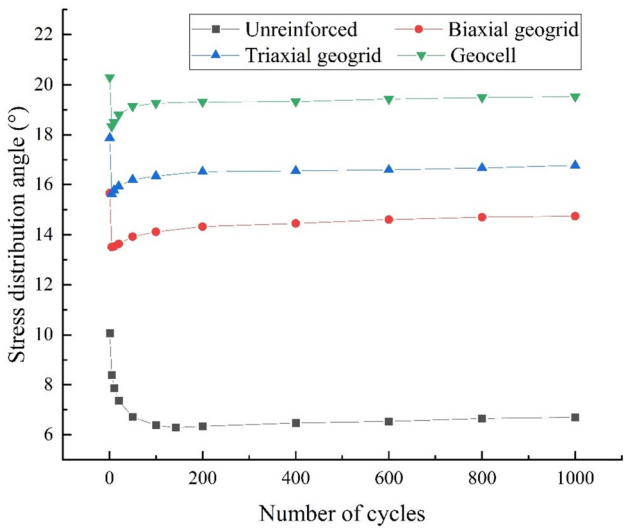

Fig. 19 Variation of stress distribution angle with number of cycles in unreinforced and reinforced subgrades

To better evaluate the impact of geosynthetics on the vertical stress in the subgrade, vertical stress was measured at different depths within the subgrade soil, and peak dynamic responses were recorded. According to Fig. 17, it can be observed that the vertical stress in the reinforced subgrade is significantly lower than that in the unreinforced subgrade, with notable differences in the reduction levels among different types of reinforced subgrades. For example, at a depth of 10 cm, the vertical stresses for biaxial geogrid, triaxial geogrid, and geocell-reinforced subgrades are reduced by approximately 22.5, 28.8, and 34%, respectively, compared to the unreinforced subgrade. This indicates that geocell effectively distributes the load over a wider area, outperforming the reinforcement effects of biaxial and triaxial geogrids. However, due to experimental constraints, the contours of vertical stress distributions in soils with different reinforcements cannot be provided, which is a noted limitation in the study. The conclusion has been supported with relevant references to substantiate the findings [29, 56, 57]. This improvement is attributed to the better lateral confinement of soil particles provided by the geocell, which enhances the overall stiffness of the subgrade. Additionally, it can be seen that vertical stress gradually decreases with depth in the soil layer. The rate of reduction in vertical stress is slower than the decrease in acceleration, with a reduction of about 90% at a depth of 0.5 m. This suggests that the influence range of vertical stress is approximately 0.7 m, which is consistent with the findings of Li et al. [46] and Li et al. [33].

In order to investigate the lateral distribution of vertical stress in the reinforced subgrade, this study monitored and compared the peak vertical stress at a depth of 10 cm at the center of the load plate, 1.0, and 2.0B under a load magnitude of 267 kPa, as shown in Fig. 18 It can be observed that the effect of load on the lateral vertical stress at the center of the load plate gradually decreases until it reaches 2.0B. Under the same load, the peak vertical stress in the reinforced subgrade is lower than that in the unreinforced subgrade, while the peak vertical stress at 1.0B from the center of the load plate is higher than that in the

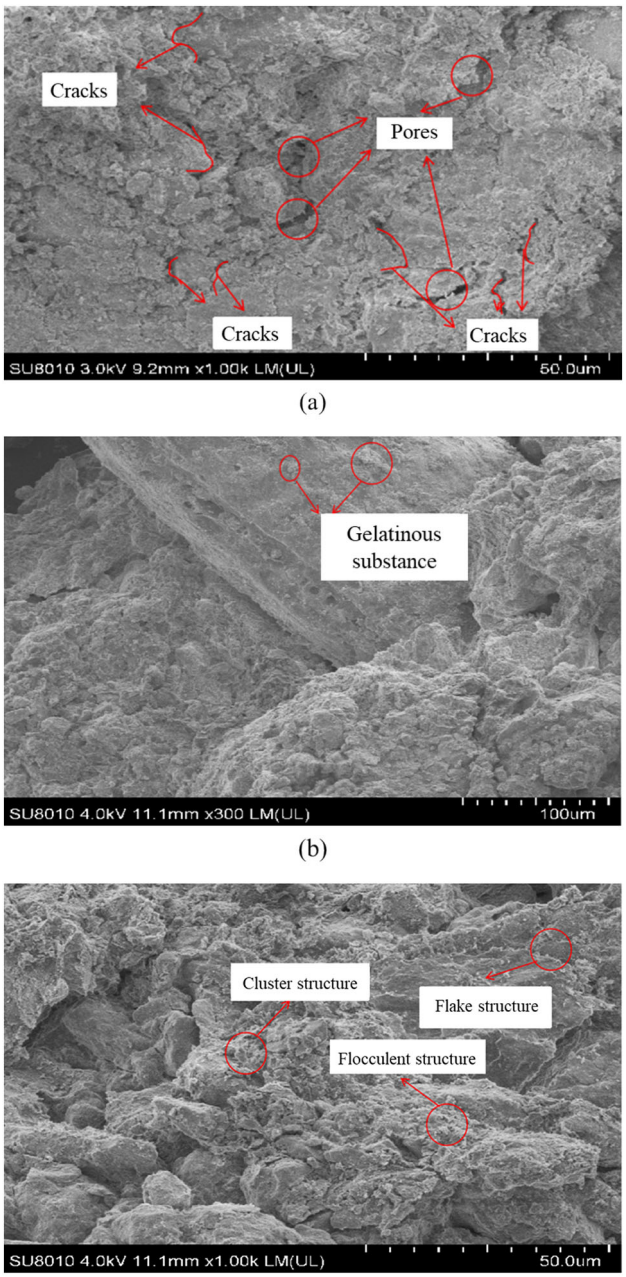

Fig. 20 SEM images: **a** 1000 times plain soil; **b** 300 times improved soil; **c** 1000 times improved soil

unreinforced subgrade. This indicates that as the applied load increases, the membrane effect gradually becomes significant, leading to a more uniform lateral distribution of vertical stress beneath the load plate. It was also found that the reinforcing effect of geocell reinforcement effect is more obvious than the geogrid reinforcement. This is because the geocell effectively distributes the load over a wider area, leading to a redistribution of additional stress and resulting in a more uniform lateral vertical stress in the geocell-reinforced subgrade. However, due to experimental constraints, the contours of stress distributions in soils with geocell reinforcement cannot be provided, which is a noted limitation in the study. The conclusion has been supported with relevant references to substantiate the findings [29, 56, 57].

3.4.4 Stress distribution angle

The ability of the reinforcement to distribute the load over a wider range can be quantified by the stress distribution angle α_{max}. The stress distribution angle refers to the maximum angle at which stress on the surface of an object spreads outward from a point, reflecting the spread of load influence [29, 55]. α_{max} can be obtained from Eq. (6)

$$\sigma_{c|max,N} = \sigma_p \times \frac{D_e^2}{(D_e + 2z\tan\alpha_{max})^2} \tag{6a}$$

$$D_e = 2\sqrt{B^2/\pi} \tag{6b}$$

where σ_p is the applied pressure, $\sigma_{c|max,N}$ is the maximum vertical stress, D_e is the diameter of the load plate, and z is the distance from the load plate to the measured position.

Figure 19 shows the variation of α_{max} with the number of cycles for both unreinforced and reinforced subgrades at a depth of 5 cm. It is evident that during the initial loading phase, the α_{max} for both unreinforced and reinforced subgrades is slightly higher. As the number of cycles increases, the stress diffusion angle first decreases and then increases. With further increases in the number of cycles, the stress distribution angle tends to stabilize. The initial decrease in the stress diffusion angle is attributed to the redistribution of stress caused by the sliding or rotation of soil particles under cyclic loading. The subsequent increase in the stress diffusion angle is due to the rearrangement of soil particles during the cyclic loading and unloading process, leading to soil densification and an increase in subgrade stiffness, which results in a reduction of vertical stress within the subgrade.

Additionally, it can be observed that for the unreinforced subgrade, the stress distribution angle is minimized at N = 143, while for the reinforced subgrade, it is minimized at N = 5. This indicates that the inclusion of geosynthetics restricts the movement of soil particles, allowing the reinforced subgrade to maintain a more uniform distribution of load. The friction between geosynthetics and soil particles may also significantly affect the stress distribution angle.

Furthermore, it is noted that in all cases, the stress distribution angle for the reinforced subgrade is higher than that for the unreinforced subgrade. The subgrade reinforced with geocell exhibits a higher stress distribution angle compared to other reinforcement types. This can be attributed to the lower vertical stress generated in the

pavement reinforced with geocell under the same load cycles. At the end of the loading cycles, the stress distribution angles for the biaxial geogrid, triaxial geogrid, and geocell-reinforced subgrades increase by 1.2, 1.5, and 1.9 times, respectively, compared to the unreinforced subgrades. Therefore, the addition of geosynthetic can distribute the load over a larger area and significantly reduce the stress levels in the subgrade.

4 Limitation

Regarding the limitations of this study, in addition to those mentioned in the main text, the test focuses on a single-layer reinforced model, whereas multilayer reinforcement is more commonly applied in engineering practice, and the mutual interactions between materials require further investigation. Moreover, the internal stability of the physical model was not analyzed in this study, representing a limitation due to the focus on bearing capacity [58, 59]. Following the research of Liu et al. [60], future work will include finite element modeling to evaluate soil–geogrid interactions, with detailed steps and results to be developed and reported in later research.

Additionally, this study presents numerous test results, but the data lack comprehensive quantitative analysis, including detailed static and dynamic evaluations. This represents a key limitation of the current work. To address this, future studies will focus on incorporating advanced quantitative methods, such as statistical modeling and in-depth static analysis, to enhance the robustness and interpretability of the findings.

5 Conclusion

This study investigated the use of fly ash and coir fiber as novel sustainable waste materials to improve expansive soil subgrades. Through a series of compaction tests and unconfined compressive strength tests, the optimal proportions of fly ash and coir fiber were determined. Additionally, physical model tests were conducted to study the reinforcement effects of different geosynthetics on the improved expansive soil subgrades. The following conclusions were drawn.

(1) The maximum dry density of the fly ash-soil mixture first increases and then decreases with increase in fly ash content. The optimum moisture content of the improved soil is at its minimum when the fly ash content is 20%, which corresponds to the maximum dry density. The addition of fly ash enhances the unconfined compressive strength of the improved expansive soil, with the highest strength achieved at 20% fly ash content. Furthermore, the inclusion of coir fiber significantly increases the unconfined compressive strength of the composite improved expansive soil, with the peak strength observed at 0.5% coir fiber content. Test results indicate that the combination of 20% fly ash and 0.5% coir fiber is the most effective for treating expansive soils and can be considered the optimum ratio.

(2) According to the static loading test results, the bearing capacity of geosynthetic-reinforced subgrades can be improved by 70–88% compared to unreinforced subgrades. The optimal embedment depth for geosynthetics is approximately 0.33 times the foundation width. The improvement factor (IF) of the reinforced subgrade increases with the increase in subgrade settlement. For any given foundation settlement, the IF values for the reinforced subgrades are ranked in descending order as follows: biaxial geogrid reinforcement, triaxial geogrid reinforcement, and geocell reinforcement.

(3) In the dynamic loading tests, the rate of change in cumulative settlement gradually decreases with the increase in the number of cycles, eventually reaching a relatively stable state. The settlement of the load plate increases with the amplitude of the cyclic load. The peak and trough values of acceleration occur in pairs, with a response frequency that matches the loading frequency. Both the settlement and vibration (acceleration) of the reinforced subgrade are lower than those of the unreinforced subgrade. The effect of geocell reinforcement is more pronounced than that of geogrid reinforcement.

(4) As the load magnitude increases, the vertical stress within the subgrade also increases. The vertical stress gradually decreases with depth in the soil layer, with the rate of decrease in the vertical direction being slightly slower than that in the acceleration direction. The effect of the applied load on the horizontal vertical stress diminishes until reaching a distance of 2.0B from the center of the load plate. With an increase in the number of cycles, the stress distribution angle of the subgrade first decreases and then increases, ultimately stabilizing. The vertical stress in the reinforced subgrade is significantly lower than that in the unreinforced subgrade, while the stress distribution angle in the reinforced subgrade is higher than that in the unreinforced subgrade. Compared to geogrid reinforcement, the stress distribution angle in the geocell-reinforced subgrade is even higher.

Appendix 1. Scanning electron microscope (SEM) results

The SEM results are given in Fig. 20, revealing detailed microstructural changes in the soil samples. Figure 20 (a) displays many pores and cracks in the soil sample. As shown in Fig. 20 (b) and (c), the addition of fly ash mainly undergoes a hydration reaction with volcanic ash, creating gelatinous substances with flake and cluster structures. These products stick to the soil particle surfaces and fill the spaces between particles, thus improving soil compaction, strengthening the soil framework, and ultimately boosting overall soil strength. Sudhakaran et al. [61] observed that untreated soil samples contained a large number of pores, while treated soil samples formed cementitious compounds during curing, making the microstructure more compact; Anggraini et al. [62] observed that the surface of coconut fiber treated with lime became rougher, which was more conducive to bonding.

As shown in Fig. 20c, the addition of coir fiber results in the partial removal of the outer layer on the fiber surface, revealing clear and orderly pits, while the rough surface of the coconut shell fibers exhibits the growth of gelatinous substances, indicating a positive effect from their incorporation. Coir fibers serve two primary functions: firstly, they guide the distribution of hydration products within the soil matrix, creating an optimal environment for these materials to develop, with the resulting adhesive compounds binding the soil and fibers to reinforce the soil structure effectively; secondly, the rough texture of the coconut shells enhances friction with soil components under mechanical stress, acting as a structural constraint to resist deformation of the soil mass [63, 64]

Acknowledgements The authors gratefully acknowledge the financial support from the National Natural Science Foundation of China (Grant No. 52278347), the Natural Science Fund for Creative Groups of Hubei Province (Grant No. 2024AFA009), the Outstanding Young and Middle-aged Scientific and Technological Innovation Team Project of Higher Education Institutions in Hubei Province (Grant No.T2023006), and the Joint Funds of the National Nature Science Foundation of China (No. U22A20232).

Funding Open access funding provided by The Hong Kong Polytechnic University. Funding was by the National Natural Science Foundation of China (Grant No. 52278347), Natural Science Fund for Creative Groups of Hubei Province (Grant No. 2024AFA009), Outstanding Young and Middle-aged Scientific and Technological Innovation Team Project of Higher Education Institutions in Hubei Province (Grant No. T2023006), Joint Funds of the National Nature Science Foundation of China (Grant No. U22A20232).

Declarations

Conflict of interest The authors declare that they have no known competing financial interests or personal relationships that could have appeared to influence the work reported in this paper.

References

1. Liu C, Lu K, Wu Z, Liu X, Garg A, Qin Y, Mei G, Lv C (2024) Expansive soil improvement using industrial bagasse and low-alkali ecological cement. Constr Build Mater 423:135806
2. Punthutaecha K, Puppala AJ, Vanapalli SK, Inyang H (2006) Volume change behaviors of expansive soils stabilized with recycled ashes and fibers. J Mater Civ Eng 18:295–306
3. Rosenbalm D, Zapata CE (2017) Effect of wetting and drying cycles on the behavior of compacted expansive soils. J Mater Civ Eng 29:04016191
4. Tiwari N, Satyam N, Puppala AJ (2021) Strength and durability assessment of expansive soil stabilized with recycled ash and natural fibers. Transp Geotech 29:100556
5. Zornberg JG, Azevedo M, Sikkema M, Odgers B (2017) Geosynthetics with enhanced lateral drainage capabilities in roadway systems. Transp Geotech 12:85–100
6. Du Y, Li S, Hayashi S (1999) Swelling–shrinkage properties and soil improvement of compacted expansive soil, Ning-Liang Highway, China. Eng Geol 53:351–358
7. Estabragh A, Rafatjo H, Javadi A (2014) Treatment of an expansive soil by mechanical and chemical techniques. Geosynth Int 21:233–243
8. Zha F, Qiao B, Kang B, Xu L, Chu C, Yang C (2021) Engineering properties of expansive soil stabilized by physically amended titanium gypsum. Constr Build Mater 303:124456
9. Behnood A (2018) Soil and clay stabilization with calcium-and non-calcium-based additives: a state-of-the-art review of challenges, approaches and techniques. Transp Geotech 17:14–32
10. Talluri N, Puppala AJ, Congress SS, Banerjee A (2020) Experimental studies and modeling of high-sulfate soil stabilization. J Geotech Geoenviron Eng 146:04020019
11. Chenarboni HA, Lajevardi SH, MolaAbasi H, Zeighami E (2021) The effect of zeolite and cement stabilization on the mechanical behavior of expansive soils. Constr Build Mater 272:121630
12. Ali N, Jaffar A, Anwer M, Khan S, Anjum M, Hussain A, Raja M, Ming X (2015) The greenhouse gas emissions produced by cement production and its impact on environment: a review of global cement processing. International Journal of Research (IJR) 2
13. Crawford RH (2022) Greenhouse gas emissions of global construction industries IOP Conference Series: Materials Science and Engineering IOP Publishing, Bristol pp. 012047.
14. Sivapullaiah P, Prashanth J, Sridharan A (1996) Effect of fly ash on the index properties of black cotton soil. Soils Found 36:97–103
15. Cokca E (2001) Use of class c fly ashes for the stabilization of an expansive soil. J Geotech Geoenvironmental Eng 127:568–573

16. Phani Kumar B, Sharma RS (2004) Effect of fly ash on engineering properties of expansive soils. J Geotech Geoenviron Eng 130:764–767
17. Zha F, Liu S, Du Y, Cui K (2008) Behavior of expansive soils stabilized with fly ash. Nat Hazards 47:509–523
18. Li L, Zhang H, Xiao H, Pei Y, Wang J (2023) Mechanical and microscopic properties of alkali-activated fly-ash-stabilised construction and demolition waste. Eur J Environ Civil Eng 27:2661–2677
19. Diambra A, Ibraim E (2014) Modelling of fibre–cohesive soil mixtures. Acta Geotech 9:1029–1043
20. Koci P, Foster CD (2023) A fiber-reinforced constitutive model for earthen materials. Acta Geotech 18:279–298
21. Kou H-l, Liu J-h, Guo W, Hua S-d, Pan Y-t (2021) Effect of freeze–thaw cycles on strength and ductility and microstructure of cement-treated silt with polypropylene fiber. Acta Geotech 16:3555–3572
22. Zhou L, Chen J-F, Zhuang X-Y (2023) Undrained cyclic behaviors of fiber-reinforced calcareous sand under multidirectional simple shear stress path. Acta Geotech 18:2929–2943
23. Sivakumar Babu G, Vasudevan A (2008) Strength and stiffness response of coir fiber-reinforced tropical soil. J Mater Civ Eng 20:571–577
24. Sivakumar Babu G, Vasudevan A, Sayida M (2008) Use of coir fibers for improving the engineering properties of expansive soils. J Nat Fibers 5:61–75
25. Maliakal T, Thiyyakkandi S (2013) Influence of randomly distributed coir fibers on shear strength of clay. Geotech Geol Eng 31:425–433
26. Anggraini V, Asadi A, Huat BB, Nahazanan H (2015) Effects of coir fibers on tensile and compressive strength of lime treated soft soil. Measurement 59:372–381
27. Wang J-Q, Zhang L-L, Xue J-F, Tang Y (2018) Load-settlement response of shallow square footings on geogrid-reinforced sand under cyclic loading. Geotext Geomembr 46:586–596
28. Li L, Cui F, Ferreira P, Xiao H, Jie H (2019) Experimental study of embankments with different reinforcement materials and spacing between layers. Geotext Geomembr 47:477–482
29. Baadiga R, Balunaini U, Saride S, Madhav MR (2021) Influence of geogrid properties on rutting and stress distribution in reinforced flexible pavements under repetitive wheel loading. J Mater Civ Eng 33:04021338
30. Raja MNA, Shukla SK (2021) Experimental study on repeatedly loaded foundation soil strengthened by wraparound geosynthetic reinforcement technique. J Rock Mech Geotech Eng 13:899–911
31. Hussain M, Dash SK (2016) The influence of lime on the compaction behaviour of soils. Environ Geotech 3:346–352
32. Puppala A J, Mohammad L N, & Allen, A (1996) Engineering behavior of lime-treated Louisiana subgrade soil. transportation research record, 1546(1): 24–31
33. Li J, Chen S, Yu F, Dai Z, Ojekunle OV (2020) In situ model tests to investigate the dynamic response of water-softened subgrade under vibrating loads. Soil Dyn Earthq Eng 138:106336
34. Li L, Xiao H, Gao M, Liu Y, Hu Z, Yao K (2019) Experimental investigations on effect of geocell, waste tire chips, and geocell–tire chips on foundation reinforcement. J Perform Constr Facil 33:04019074
35. Macagno EO (1971) Historico-critical review of dimensional analysis. J Franklin Inst 292:391–402
36. Huang Q, Geng X, Ren F (2025) Connection failure between reinforcement and facing in geosynthetic reinforced soil bridge abutments: a case study. Geotextiles Geomembr 53:974–984
37. Mehrjardi GT, Khazaei M (2017) Scale effect on the behaviour of geogrid-reinforced soil under repeated loads. Geotext Geomembr 45:603–615
38. Sharma V, Akhil T, Saha G (2023) Life Cycle Cost Analysis and Performance Evaluation of Flexible Pavements Using Geogrid in Soil Subgrade. International Conference on Innovative Methods and Practical Applications for Cognizant Transportation Systems. Singapore, Springer Nature Singapore, pp 303–316
39. Mahdi SN, Imjai T, Wattanapanich C, Garcia R, Kaur H, Musarat MA (2023) Life cycle cost analysis of flexible pavements reinforced with geosynthetics: a case study of new construction or repair overlays in Thailand's roads. Engineered Sci 28:1071
40. Poorahong H, Jamsawang P, Thanasisathit N, Jongpradist P, Horpibulsuk S (2024) Enhancing the bearing capacity of unpaved roads on soft clay subgrade using geogrid reinforcement with a triaxial configuration. Constr Build Mater 456:139321
41. Tafreshi SM, Dawson AR (2010) Comparison of bearing capacity of a strip footing on sand with geocell and with planar forms of geotextile reinforcement. Geotext Geomembr 28:72–84
42. Lal D, Sankar N, Chandrakaran S (2017) Effect of reinforcement form on the behaviour of coir geotextile reinforced sand beds. Soils Found 57:227–236
43. Zhan ZQ, Zhou C, Cai GL, Liu CQ, Liu JQ, Wu Y (2026) Physical and MPM modelling of sand column collapse with different moisture and density conditions. Powder Technol 467:121572. https://doi.org/10.1016/j.powtec.2025.121572
44. Li L, Li J, Zhan Z, Gui Y, Liu J (2025) Experimental analysis of reinforcement methods for stone column foundations. Soils Found 65(4):101661. https://doi.org/10.1016/j.sandf.2025.101661
45. Li-Hua L, Shuai-Shuai L, Heng-Lin X, Wei-Qiang F, Jun-Peng L, Pei-Chen W (2022) Experimental investigation on reinforcement effect of sustainable materials for different subgrades. J Clean Prod 343:130944
46. Li J, Chen S, Yu F, Dai Z (2018) Remote monitoring for a high-speed railway subgrade structure state in a mountainous area and its response analysis. Bull Eng Geol Env 77:409–427
47. Chaple PM, Dhatrak A (2013) Performance of coir fiber reinforced clayey soil. Int J Eng Sci 2:54–64
48. Soundara B (2015) Effect of fibers on properties of clay. Int J Eng Appl Sci 2:257909
49. Liu J, Pan J, Wang B, Hu C, Liu Q (2024) Study on the shear and deformation characteristics of geogrid-reinforced gravelly soils based on large-scale triaxial tests. Front Earth Sci 12:1287718
50. Shukla S, Sivakugan N, Das B (2011) A state-of-the-art review of geosynthetic-reinforced slopes. Int J Geotech Eng 5:17–32
51. Mittal RK, Gill G (2018) Sustainable application of waste tire chips and geogrid for improving load carrying capacity of granular soils. J Clean Prod 200:542–551
52. Banerjee S, Manna B, Shahu J (2024) Experimental investigation of the geometry of geocell on the performance of flexible pavement under repeated loading. Geotext Geomembr 52:654–670
53. Juneja G, Sharma RK (2023) Experimental and numerical analysis of geocell-reinforced base layer with different infill materials overlying clay. J Hazard Toxic Radioact Waste 27:04023024
54. Khan R, Latha GM (2025) Multi-scale behaviour of sand-geosynthetic interactions considering particle size effects. Geotext Geomembr 53:169–187
55. Qian Y, Han J, Pokharel SK, Parsons RL (2013) Performance of triangular aperture geogrid-reinforced base courses over weak subgrade under cyclic loading. J Mater Civ Eng 25:1013–1021
56. Pokharel SK, Han J, Leshchinsky D, Parsons RL, Halahmi I (2010) Investigation of factors influencing behavior of single geocell-reinforced bases under static loading. Geotext Geomembr 28:570–578
57. Thakur JK, Han J, Pokharel SK, Parsons RL (2012) Performance of geocell-reinforced recycled asphalt pavement (RAP) bases over weak subgrade under cyclic plate loading. Geotextiles Geomembr 35:14–24

58. Collin JG, Stark TD, Lucarelli A, Taylor TP, Berg RR (2021) Stability and stress-deformation analyses of reinforced slope failure at Yeager Airport. J Geotech Geoenviron Eng 147:04020179
59. Morsy AM, Zornberg JG, Leshchinsky D, Christopher BR, Han J, Tanyu BF (2020) Experimental evaluation of the interaction among neighboring reinforcements in geosynthetic-reinforced soils. J Geotech Geoenviron Eng 146:04020107
60. Liu H, Wang X, Song E (2011) Reinforcement load and deformation mode of geosynthetic-reinforced soil walls subject to seismic loading during service life. Geotext Geomembr 29:1–16
61. Sudhakaran SP, Sharma AK, Kolathayar S (2018) Soil stabilization using bottom ash and areca fiber: experimental investigations and reliability analysis. J Mater Civ Eng 30:04018169
62. Anggraini V, Asadi A, Farzadnia N, Jahangirian H, Huat BB (2016) Reinforcement benefits of nanomodified coir fiber in lime-treated marine clay. J Mater Civ Eng 28:06016005
63. Shenal Jayawardane V, Anggraini V, Emmanuel E, Yong LL, Mirzababaei M (2020) Expansive and compressibility behavior of lime stabilized fiber-reinforced marine clay. J Mater Civ Eng 32:04020328
64. Syed M, Ahuja M, Jambholkar AR, GuhaRay A (2022) Laboratory investigation on fiber-reinforced expansive subgrade soil stabilized with alkali activated binder: a reliability-based perspective Geo-Congress 2022, pp. 241-250.